



Isolating the effects of surface roughness versus wall shape in numerically optimized, additively manufactured micro cooling channels

Kathryn L. Kirsch*, Karen A. Thole

Pennsylvania State University, University Park, PA 16802, USA

ARTICLE INFO

Keywords:

Microchannel cooling
Additive manufacturing
Laser Powder Bed Fusion
3D printing
Shape optimization
Computational fluid dynamics
Heat transfer

ABSTRACT

Metal-based additive manufacturing is a disruptive technology with the capability to transform industries. The increased design space the technology offers is enticing to designers, who are given an opportunity to develop components that exceed prior performance levels; optimization tools can be used to provide guidance. However, the nature of surface roughness in additively manufactured parts is highly irregular, and computational models generally cannot properly capture the surface morphology. How, then, can current numerical tools predict the performance of additively manufactured components, or aid designers in developing products that meet their needs?

The current study aims to provide insight into the current capabilities of both design tools and the additive manufacturing process for microchannels intended for cooling components. A commercially-available optimization scheme was used to improve the design of four microchannel cooling configurations. These optimized geometries were printed using a metal-based additive manufacturing process; only some objective functions were achieved experimentally. In the current study, the same optimized geometries were printed using a stereolithography process, which built smooth channels as simulated in the optimization scheme. Experiments were performed to gather friction factor data, and results showed that the design intents were largely validated. Analyses of the metal test coupons alongside the plastic coupons showcase the direct effects of surface roughness: the influence of surface roughness on the performance of the channels was predominantly tied to the goal of the shape change.

1. Introduction

Additive manufacturing (AM) has generated widespread excitement for a variety of applications. The advanced manufacturing technique can create near net shape geometries, including at the micro-scale, and its applications range from prototypes to production-level components.

Building parts layer-by-layer lifts many design constraints imposed by conventional, subtractive manufacturing techniques. As such, the true potential of AM can only be realized when this more open design space is fully exploited: numerical design tools are a necessary component in the ever-evolving field of AM. However, the current connection between computational models and their as-built counterparts can be weak, depending on the manufacturing method used.

Metal-based AM, for example, is one such process that produces parts that can deviate from their design intent given the complexity of the manufacturing process. Especially at the micro-scale, poor surface finish in metal AM parts affects not only the success of the build to replicate the intended design accurately, but also the ability of the part

to function as desired. Evaluating the effectiveness of design tools for metal AM, therefore, can be difficult; upon analyzing the performance of the as-built parts, a natural question arises as to whether the performance can be attributed to the design features, or simply to the resultant geometry.

The current study seeks to isolate the effects of design features from surface roughness in parts created through Laser Powder Bed Fusion (L-PBF), one type of metal AM. The medium through which this study will be presented is through microchannel heat exchangers. Previous work by Kirsch and Thole [1,2] found mixed success in the ability of optimized L-PBF wavy microchannel designs to perform as intended. To probe deeper into those findings, the current study presents the same baseline and optimized wavy channel designs from Kirsch and Thole [1,2], but built using a Stereolithography (SLA) process, which faithfully reproduced the optimized geometries with relatively smooth surfaces. The SLA test coupons were then tested for friction factor over a range of Reynolds numbers. The results of the current study aim to interrogate the chosen optimization method, an efficient and simple

* Corresponding author.

E-mail address: kathryn.kirsch@psu.edu (K.L. Kirsch).

design tool, as well as to gain a better understanding of the effects of surface roughness in complex channels.

2. Review of relevant literature

The use of numerical tools to guide design decisions has become an integral step in the modern design process. Optimization schemes, in particular, are of distinct interest in cases where the most effective design may not be obvious, or where an acceptable compromise between competing objectives is desired. Martinelli and Jameson [3] published a detailed review of the natural relation between shape optimization and aerodynamics, the first foray into which occurred once computational fluid dynamics (CFD) became well-established.

Shape and topology optimization methods have been the focus of a number of recent studies in the field of heat exchangers [1,4–11]. Both schemes are accomplished through gradient-based optimization, meaning that the gradient of the objective function with respect to any design variables must be calculable. An efficient way to calculate this gradient for a large number of design variables is through the adjoint method, which decouples any perturbations to design variables from the flow solver.

Many studies on optimization schemes are numerical in nature [5–11]; some studies, however, have experimentally investigated their numerically optimized designs [1,4]. Dede et al. [4] used topology optimization for a finned, external-flow heat exchanger; Kirsch and Thole [1,2] used shape optimization in internal micro cooling channels. In both studies, the heat exchangers were built using L-PBF, and both authors reported that the surface finish affected their aerothermal performance. In Dede et al. [4], the optimized heat exchanger outperformed the baseline, while in Kirsch and Thole [1], the optimized channels showed mixed success relative to their baselines.

In general, external flow features can be smoothed, but internal cooling channels with large L/D are difficult to smooth while maintaining nominal channel dimensions. Seminal studies by Snyder et al. [12] and Stimpson et al. [13] reported on the effects of roughness in L-PBF microchannels. The authors found that the size of the roughness features relative to the channel hydraulic diameter played a key role in the channels' performance. Higher relative roughness directly correlated with higher friction factors, but only proved beneficial to the heat transfer to a point; once the friction factor augmentation in the channel surpassed a value of four, no further benefit to the heat transfer was realized. These results corroborated the findings from Norris [14].

The type of surface roughness that results from the L-PBF process is irregular in shape and size [15,16]. Build direction exerts a strong influence on the roughness levels [17,18], as well as the likelihood that a part will build close to its intended design [12]. Modeling such surface roughness, however, is difficult. Results from studies on the effects of uniform roughness [19–21] cannot be applied to channels in which the surface morphology is so complex. In one study by Stimpson et al. [22], however, the authors developed a correlation for predicting the friction factor and heat transfer from straight L-PBF microchannels; a key finding was that randomly roughened surfaces correlate best with the measured arithmetic mean roughness.

The channel design in the current study is one commonly used in low mass flow applications, such as those for fluid mixing or small electronics cooling. Wavy channels promote mixing in the flow due to characteristic vortical structures that form because of the centripetal force enacted on the fluid particles [23]. Common methods to create the channel waviness can be through sinusoidal waves [24,25], or from circular arcs [23]. The most common variables to change in wavy channels are the wavelength and amplitude [26,27], which affect the vortex characteristics in the channels.

Most wavy channels from the literature were performed at low Reynolds numbers ($Re < 1000$). However, studies by Kirsch and Thole [28] and Weaver et al. [29] investigated wavy channels at higher ($2000 < Re < 20000$) Reynolds numbers, and found that the benefits

of the wavy channel design transferred well to higher Reynolds number applications.

The current study is unique in that it delves into the flow physics of complex, optimized microchannel cooling designs. Until a closer tie between numerical optimization techniques and manufacturing capabilities exists, fundamental studies like the current one are crucial in bridging the gap between simulations and experiments. This study aims to explore the current capabilities of a simple, computationally-inexpensive design tool, as well as lend insight into key differences to expect between smooth and roughened channels.

3. Channel design

The wavy channels in the current study were created by sweeping a rectangle along a path constructed with four 45° arcs. This design was chosen such that the fluid particles in the channels traveled through the same radius of curvature, and thus experienced the same magnitude of centripetal force; the direction of that centripetal force switched signs from positive to negative twice in every period.

In two of the baseline configurations, the channels were isolated from one another. In the other two baseline designs, branches connected the primary channels in an effort to increase fluid mixing. Each of the isolated and communicating channel designs contained two different wavelengths, λ , relative to the entire test coupon channel length, L : $\lambda = 0.1 L$ and $\lambda = 0.4 L$.

Fig. 1 explains how the isolated wavy channel was created in the $\lambda = 0.1 L$ case; the method was the same for the $\lambda = 0.4 L$ case, therefore creating a larger amplitude wave. Ten periods were present in the $\lambda = 0.1 L$ case, while 2.5 were present for the $\lambda = 0.4 L$ case. The direction of the radius of curvature switched signs in between the peaks and troughs of the channels.

Fig. 2 shows the channel construction for the communicating wavy channels. The branches between primary channels in Fig. 2 emanated at a 45° angle to the horizontal. Branches were included in every other period in the axial dimension, and between every other channel in the spanwise dimension. This alternating pattern can be seen in the full-length image of the channels. The entrance to the branches was filleted to minimize losses, while the exit from the branch was sharper to encourage jet penetration.

4. Simulation setup

A wall-resolved, structured mesh was created for each of the four baseline configurations using the commercial grid generation software POINTWISE [30]. The y^+ values were near or below one, as is appropriate for the sublayer resolved turbulence model. The steady RANS and energy equations were solved using the realizable $k-\epsilon$ turbulence model in the CFD software FLUENT [31]; only the fluid domains were included in the simulation. The boundary conditions mimicked those from the experimental setup in Kirsch and Thole [1]; a constant temperature boundary condition was imposed on the channel top and bottom end-walls, and the flow conditions were for a Reynolds number of 5000. To validate the choice of the realizable $k-\epsilon$ turbulence model, simulations were performed on a straight, smooth, rectangular channel, whose dimensions matched those at the inlet to the wavy channels. The simulation results from the straight smooth channel matched the Colebrook formula [32] and the Gnielinski correlation [33] to within 7%.

In the case of the isolated channels, the mesh contained 1.1 million nodes. For the communicating channels, two neighboring channels were modeled with their corresponding branches, and thus contained double the number of nodes. For the communicating channels, the exterior branches were subject to periodic boundary conditions.

A grid sensitivity study was performed on one wavelength from each of the isolated and communicating channel configurations; the number of cells was doubled for the grid sensitivity study. For both cases, the change in friction factor was -0.1% from the initial grid to

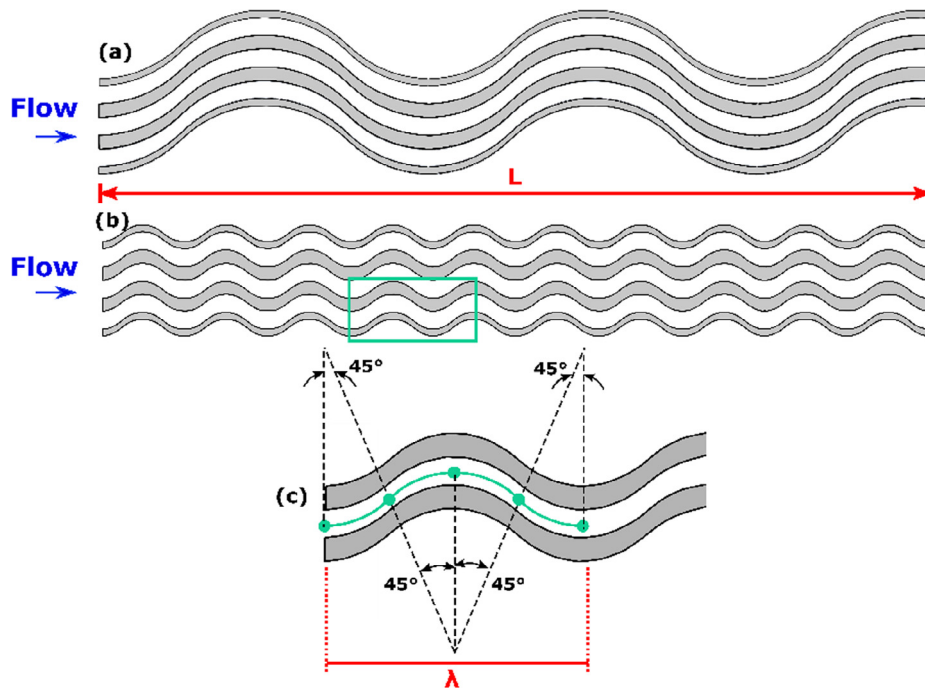


Fig. 1. Isolated wavy channel construction [1]. To create the channels, a rectangle was swept along the path created by the four 45° arcs. (a) $\lambda = 0.4L$ case, (b) $\lambda = 0.1L$ case, (c) description of wavy channel construction.

the refined grid at a Reynolds number of 5000. The change in Nusselt number for both cases was 0.1%. The initial grid size, therefore, was taken to be sufficient. Convergence was deemed acceptable when normalized residuals reached $1e-6$, which typically occurred around 4000 iterations.

Fig. 3 shows a slice of the computational mesh for the $\lambda = 0.1L$ communicating case, along with certain boundary conditions

highlighted. Note that the other computational meshes were similar. The results from the numerical simulation fed into a shape optimization analysis, which was embedded within the same program as the flow solver [31]. Shape optimization was accomplished through a sensitivity analysis, which was calculated by solving a set of equations known as the adjoint equations. The adjoint method is a highly efficient means of calculating the sensitivity of many design variables on a given objective

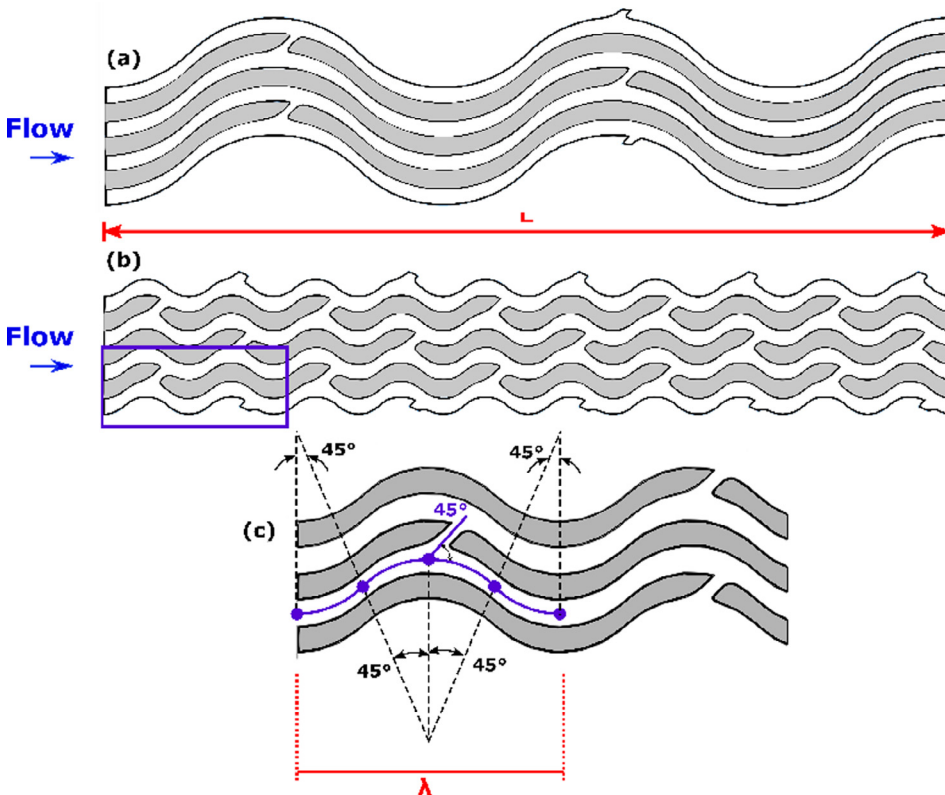


Fig. 2. Communicating wavy channel configuration [2]. The primary channels were created in the same manner as shown in Fig. 1, but branches were included to encourage fluid mixing. Branches emerged from the primary channels at a 45° angle to the horizontal. (a) $\lambda = 0.4L$ case, (b) $\lambda = 0.1L$ case, (c) description of wavy channel construction. Note the sharp corner at the branch exit, which was included to encourage jet penetration.

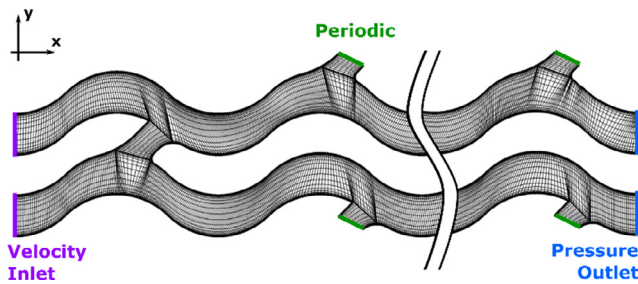


Fig. 3. Top-down view at 50% channel height of the computational mesh used for the $\lambda = 0.1L$ communicating channel configuration. In the case of the isolated channels, only one channel was included in the simulation. Not shown in this figure is the heat input into the simulation, which was accomplished through a constant temperature boundary condition on the top and bottom endwalls.

function. In the current simulation, each one of the nodes in the computational mesh represented a design variable, or a degree of freedom.

Each of the four baseline configurations were subjected to three different objective functions, denoted as J and shown in Eqs. (1)–(3). The first objective was to minimize the pressure loss between channel inlet and outlet, the second objective was to maximize the heat transfer on the top and bottom endwalls, and the third objective sought to maximize the ratio of heat transfer to pressure loss. The form of the third objective function mirrors a commonly-used performance factor in internal cooling channels, originally derived in Gee and Web [34].

$$J_1 = \min(\Delta P) \quad (1)$$

$$J_2 = \max(Q) \quad (2)$$

$$J_3 = \max\left(\frac{Q}{\Delta P^{1/3}}\right) \quad (3)$$

A full, mathematical description of the adjoint method is given in Kirsch and Thole [1]; the derivation and discretization of the adjoint equations, however, were accomplished within the program [31]. The adjoint equations are solved to convergence much like the governing equations for the flow solver. Once converged, the sensitivity of each one of the design variables (mesh nodes) on the objective at hand can be determined. The user defines the degree to which the shape should change, then the mesh is morphed as directed by the sensitivity results. The shape changes must be incremental enough that the resultant mesh retains its original quality and its original y^+ values. The flow solver governing equations are then solved to convergence with the new geometry, and the objective function can be compared to the results from the previous flow solution.

One design iteration includes solving the governing equations to convergence, solving the adjoint equation to convergence, morphing the mesh, and re-running the flow solver. In all, between six and fourteen design iterations were performed for each of the objective functions on each of the baseline designs. A final design was chosen when either the objective function no longer changed, or the flow solver no longer converged. Inability of the flow solver to converge was generally due to a poor quality mesh that emerged from the mesh morphing stage; an example scenario would be if the sensitivity analysis forced a shape change that resulted in negative cell volumes. Mesh quality, therefore, imposed an implicit constraint on the shape optimization process.

Each of the shape changes achieved their intended objective function. Table 1 shows the results from the numerical study of the non-communicating channels as a percentage of the baseline value; Table 2 shows the same data, but from the communicating channel configuration. The bolded values show the results from the objective function at hand, while the other two values are shown for comparison.

In general, the objective to maximize heat transfer was the most

Table 1
Changes in ΔP , Q , and $Q/\Delta P^{1/3}$ in non-communicating optimized channels relative to each respective baseline.

	$\lambda = 0.1L$			$\lambda = 0.4L$		
	ΔP	Q	$Q/\Delta P^{1/3}$	ΔP	Q	$Q/\Delta P^{1/3}$
J_1	−8.4%	−0.5%	+2.5%	−5.5%	−3.5%	−1.6%
J_2	+28.5%	+26%	+16%	+7%	+5.3%	+3%
J_3	+1.7%	+23.8%	+17.5%	+4.8%	+4.8%	+3.2%

Table 2
Changes in ΔP , Q , and $Q/\Delta P^{1/3}$ in communicating optimized channels relative to each respective baseline.

	$\lambda = 0.1L$			$\lambda = 0.4L$		
	ΔP	Q	$Q/\Delta P^{1/3}$	ΔP	Q	$Q/\Delta P^{1/3}$
J_1	−4.4%	−3.9%	−2.5%	−3.2%	+0.2%	+1.3%
J_2	+6.6%	+6.6%	+4.3%	+11.7%	+11.7%	+6.6%
J_3	+0.4%	1.9%	+1.8%	+3.3%	+1.8%	+2.7%

successful. Perhaps because the wavy channel configuration already promoted such strong mixing in the flow, this objective was easiest to satisfy. The most significant deviation from the baseline was seen in the $\lambda = 0.1L$ non-communicating channel to maximize heat transfer (+26%). By contrast, the least significant deviations from the baseline were seen in the objectives to maximize the ratio of heat transfer to pressure loss for both wavelengths in Table 2, which shows the communicating channels. The conflict between increasing the heat transfer and decreasing the pressure loss was not well-resolved by the optimizer in the communicating channels.

5. Optimized geometries

The shape changes that occurred for each of the optimized geometries were aperiodic; in general, the most significant shape changes for both the isolated and communicating channels came in the streamwise middle of the channel. A high-level discussion of the shape changes will be given here, while a more in-depth discussion on the shape changes, and their resulting flow patterns, will be included in Section 7.

In the isolated channels, all shape changes took place in between the peaks and troughs of the channels, while the cross-sectional shape at the peaks and troughs remained rectangular. Where heat transfer was to be maximized, in J_2 and J_3 , the shape changes sought to promote stronger fluid mixing. As can be seen in Fig. 4, the 2D slices for the J_2 and J_3 cases show an increase in cross-sectional area before the approaching trough; after the trough came a decrease in the cross-sectional area. This alternating pattern of increased, then decreased, cross-sectional area roughly repeated itself along the channel. The result of this pattern was the formation of stronger vortical structures than was seen in the baseline case, as evidenced by both the magnitude and direction of the secondary velocity vectors shown in Fig. 4.

In the case of J_1 , where the objective was to minimize pressure loss, the shape changes sought to minimize any backflow in the channels. This intention can be seen in Fig. 4, especially in the 2D slices beyond the trough. The cluster of velocity vectors seen on the left (from the reader's point of view) wall of the baseline case are not seen in the J_1 case. Indeed, the shape changes for the J_1 objective were more modest than those for the J_2 and J_3 cases, the consequences of which are noted in Table 1: the change in ΔP from the baseline was less than the changes in either Q or $Q/\Delta P^{1/3}$.

The communicating channels saw the most significant shape changes in and surrounding the branches. In general, where heat transfer was to be maximized, shape changes in the branches sought to encourage jet penetration into the neighboring channel. Conversely,

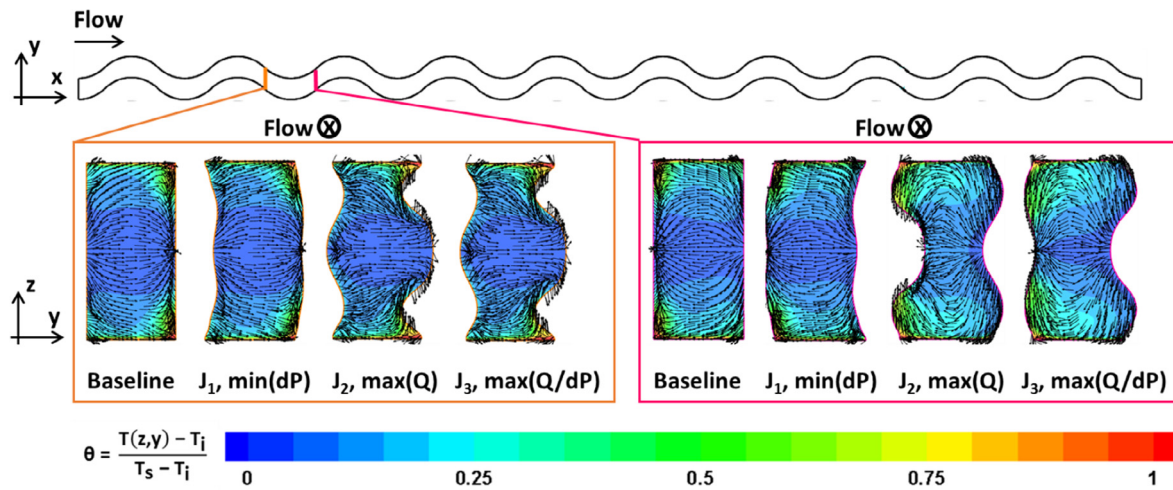


Fig. 4. 2D slices showing shape changes for the $\lambda = 0.1 L$ isolated channel design. Secondary velocity vectors are superimposed on nondimensional temperature contours.

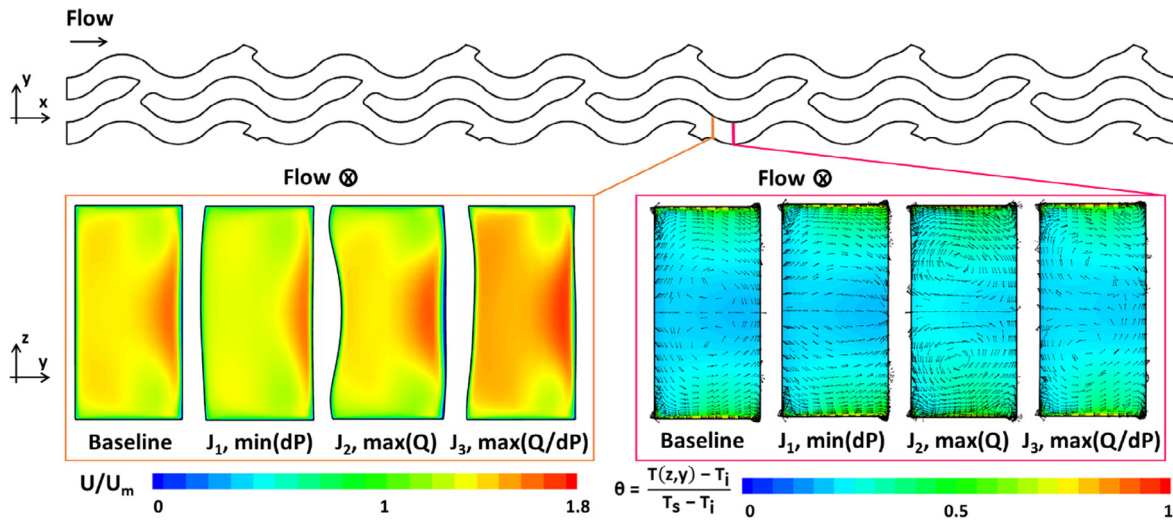


Fig. 5. 2D slices at two streamwise locations of the communicating wavy channels. On the left are contours of normalized axial velocity, and on the right are contours of normalized temperature with secondary velocity vectors overlaid.

where pressure drop was to be minimized, jet penetration was reduced. This behavior can be seen on the left of Fig. 5, which shows normalized axial velocity contours immediately beyond the exit of a branch. Higher normalized velocity was seen in the J_2 and J_3 cases, whereas the opposite was seen for J_1 case. The effects of such jet penetration, or lack thereof, can be seen on the right of Fig. 5, which shows normalized temperature contours with secondary velocity vectors overlaid: more coherent vortical structures are seen in the J_2 and J_3 cases than either the J_1 or the baseline cases.

Further description of the shape changes, including those for the $\lambda = 0.4 L$ designs, can be found in Kirsch and Thole [1,2]. Additionally, a discussion of the flow physics captured by the numerical simulations will be discussed in the context of the experimental results, where applicable.

6. Test coupon manufacture

6.1. Plastic stereolithography process

Once the optimization procedure was complete, the baseline and optimized channels were duplicated to fill a test coupon. In the current study, six channels were included in the test coupons, and the scale of the coupons was chosen such that the channels could be built in one,

solid piece. A commercially-available SLA machine was used for the build [35]. Once a build had completed, the parts were removed from the build platform, cleaned using isopropyl alcohol, and cured in a UV oven. Once cured, support structures were easily broken off.

The layer thickness (resolution in the z-dimension) was $50 \mu\text{m}$; the laser spot size (resolution in the x- and y-dimensions) was $140 \mu\text{m}$. Multiple test pieces were built at the same time, but in all, five builds were required to manufacture all pieces and took approximately 200 h to complete.

The SLA test pieces were designed such that the tops of the channels were open. Therefore, any residual resin could be cleaned out, and the internal surfaces of the channels could cure evenly. During testing, a lid was placed atop the channels to seal the test section. The channels were 6.5 mm in height, and 3.25 mm in width at the entrance, which was scaled up 6.5X from the manufactured channels in Kirsch and Thole [1,2]. The L/D for all channels was 41.

6.2. Metal additive process

The test coupons for the previous studies from Kirsch and Thole [1,2] were meant to replicate heat transfer properties of the intended production-level micro-sized heat exchanger. As such, the test pieces were manufactured from stock Inconel 718 powder [36] using default

parameters in the L-PBF process [37]. In any L-PBF process, metal powder is welded together layer-by-layer until the part is complete.

For the test coupons from Kirsch and Thole [1,2], the layer thickness was 40 μm . The x-y resolution in L-PBF processes is driven by many different process parameters and, as such, difficult to quantify. However, a typical resolution can be assumed to be within a few hundred microns [38]. The total build time for the test coupons was near 40 h; the build plate, however, contained coupons other than the sixteen test coupons from Kirsch and Thole [1,2].

The L-PBF process is comparable to a welding process and imparts significant thermal stress in each of the parts. Therefore, parts must be heat treated to eliminate any residual stresses before being removed from the build plate. Once stress-relieved, a wire electro-discharge machine (EDM) was used to remove parts from the build plate. Any other support structures not removed by the EDM were manually machined off.

As previously mentioned, a natural consequence of the L-PBF process is high surface roughness. As the laser traces each subsequent slice of the part and melts the metal powder, nearby loose powder particles can become sintered to the fully-melted regions. This behavior occurs more readily on unsupported surfaces, or those in which the current layer has no solid material directly underneath. These unsupported surfaces can also deviate from the CAD model more than supported surfaces; intricate features are more difficult to replicate when loose powder, instead of fully melted material, lies directly beneath the current layer.

The build direction for the L-PBF test coupons is shown in Fig. 6, and was chosen such that most internal surfaces would build appropriately. However, given the complicated nature of the channel designs, unsupported surfaces were unavoidable and, as a result, the L-PBF test coupons deviated from the design intent in both surface finish and geometric tolerance. Surface roughness was quantified using an arithmetic mean surface roughness and was calculated to be between 15 and 25% of the measured channel hydraulic diameters.

6.3. Non-destructive evaluation

A critical part of any AM or 3D printing study comes in properly characterizing the resultant part. Two SLA test coupons were scanned

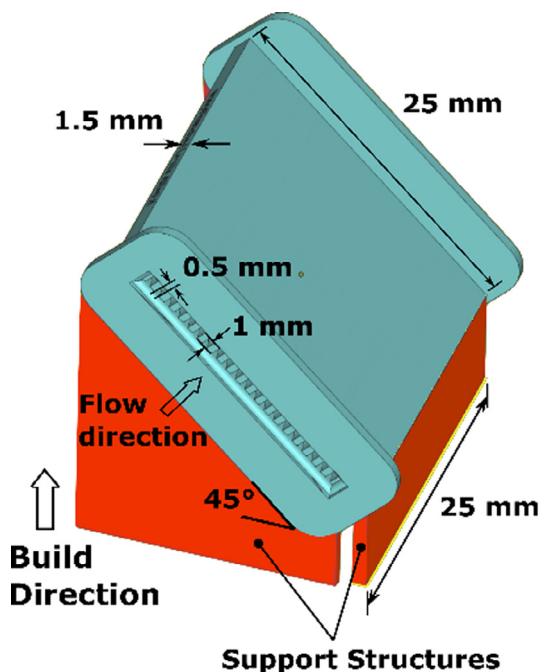


Fig. 6. Build direction for L-PBF coupons.

using X-Ray Computed Tomography (CT) to evaluate how closely the printed designs matched the optimized intent. The resolution of the scan for the plastic SLA pieces was 90 μm , which was more than sufficient to capture all design features. For both SLA test coupons, 95% of the geometry matched the CAD model to within 140 μm , the laser spot size.

Each of the L-PBF test coupons was CT scanned as well, at a resolution of 35 μm . The rough internal surfaces of the L-PBF microchannels were determined using proprietary software [39] that computed the gradient between solid material and open space. Deviations from the design were primarily driven by the roughness, although certain features such as sharp corners are inherently difficult to reproduce using L-PBF.

Fig. 7 shows a 2D slice taken at an L/D close to 7, or 17.5% the channel length for both the SLA and L-PBF channels; the intended design is shown in a black outline, while the as-built channel outlines are colored by their deviation from the CAD model. Fig. 7a shows the outline for the SLA test coupon, which was 6.5 times larger than the L-PBF test coupon, from which one channel's cross-section is shown in Fig. 7b. As such, the deviation color bar for the SLA test coupon is 6.5 times greater in magnitude than the deviation color bar for the L-PBF channels.

The deviation from the CAD model is visually much more significant in the L-PBF test coupon than in the SLA test coupon. This result is expected, given the small size of the channels. The corners of the channels in the L-PBF process did not build quite as intended, yielding much more rounded intersections between channel endwalls. However, certain design features from the optimizer were generally reproduced.

The SLA test coupon, on the other hand, built nearly identical to the design intent. The largest deviation, seen at the corners of the channel, was less than the laser spot size of 140 μm . Much of this success can be attributed to the fact that the channels were scaled up 6.5X. Given that the intent of this study was to understand how the numerical shape changes performed experimentally, the CT scan results of the SLA test coupons validated the study's premise; the SLA test coupons were deemed a sufficient representation of the optimized channel design.

6.4. Experimental setup

A bench-top rig was used to calculate the friction factor for each of the test coupons. A mass flow controller [40] governed the air flow through the test rig; the Reynolds number ranged between 2000 and 18,000. All tests were conducted at room temperature and pressure. A static pressure tap was located upstream of the channels; the channels emptied to atmosphere. During testing, vacuum grease was used to seal the interface between test piece and test section, as well as to ensure adequate contact between the channels and their lids. Fig. 8 shows a cross-section of the experimental setup. An example test piece containing the $\lambda = 0.4$ L channels is shown for reference. The test piece sits inside a lip in the test section, and the channels and their lids are clamped together to ensure no leaks occur during testing.

Mean fluid velocity was calculated from the measured mass flow rate using the cross-sectional area at the entrance to the channels; given that the SLA test pieces built so close to the design intent, the dimensions were taken to be the CAD dimensions.

To validate the test rig, a test piece containing six straight, smooth, rectangular channels was printed along with the wavy channels to test for friction factor. Fig. 9 shows the friction factor from this benchmark test coupon; outside of Reynolds numbers between 700 and 2000, the friction factor from the test coupon was within 5% of the correlations. In the laminar-to-turbulent transition region, the influence from entrance effects was measurable because of the channel L/D; Langhaar [41] found that for L/D between 20 and 63, entrance effects influenced the friction factor in the transition region.

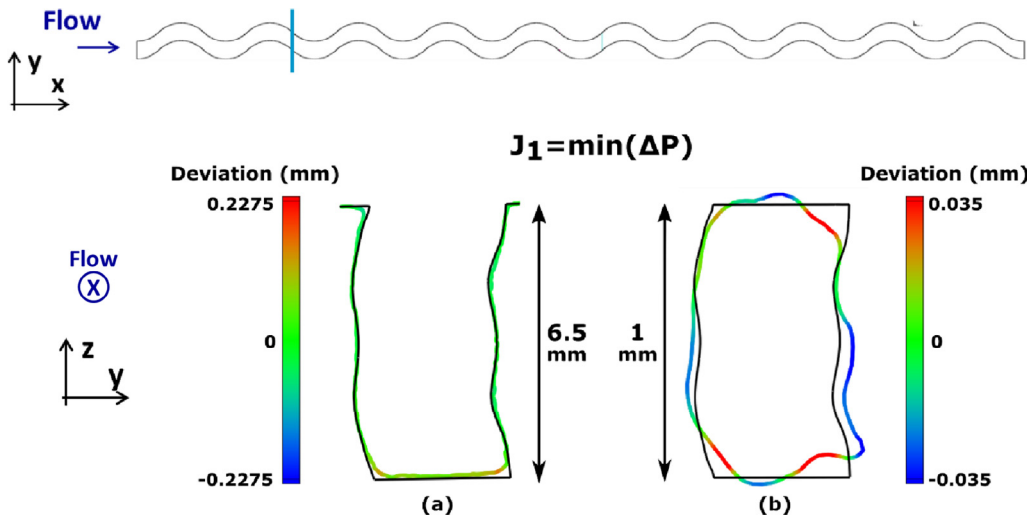


Fig. 7. Deviation from the design intent for the (a) 6.5X scale SLA test coupon and (b) the 1X scale L-PBF test coupon. The channels shown are for the objective to minimize pressure loss. The as-built channel outlines at the location specified at the top of the image are colored by their deviation from the design intent; the black outline shows the slice of the CAD model. The contour scales for the different manufacturing processes reflect the difference in scale between the two test coupons. (For interpretation of the references to colour in this figure legend, the reader is referred to the web version of this article.)

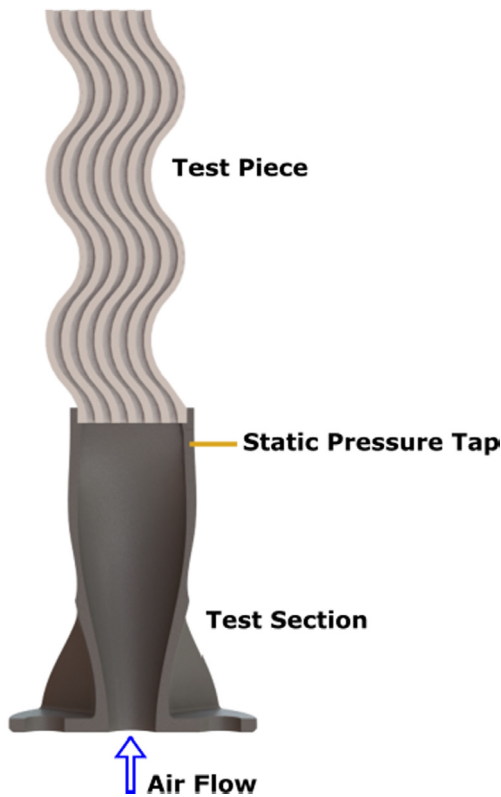


Fig. 8. Cross-section of experimental setup for friction factor tests.

6.5. Uncertainty analysis

Uncertainty was quantified using the methods proposed in Kline and McClintock [42]. Overall uncertainty in measuring friction factor was under 5% for all conditions; the largest source of uncertainty came in the calculation of the mean velocity used in the friction factor calculations. The uncertainty in measuring the pressure drop was under 0.5%, and the uncertainty in Reynolds number measurements was under 1%. Repeatability in friction factor among tests was under 4%.

7. Experimental results and discussion

Friction factor results will be presented in terms of an augmentation over a smooth baseline, calculated using the Colebrook formula [32];

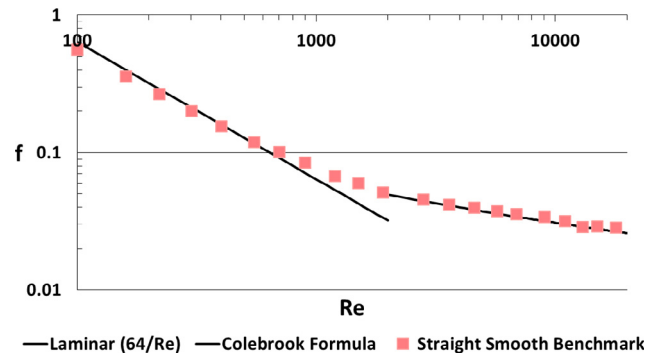


Fig. 9. Benchmarking data from straight, smooth, rectangular channels at top friction factor correlations for laminar flow ($64/Re$) and turbulent flow (Colebrook Formula).

both experimental and numerical data points will be included. Where applicable, flowfield results from the numerical simulations will be included to explain the experimental results.

7.1. SLA test coupons vs. numerical simulation

7.1.1. Non-communicating channels

Fig. 10 shows the friction factor augmentation for the SLA test coupons and the numerical results for the $\lambda = 0.1 L$ non-communicating (isolated) case. The trend with Reynolds number is constant, meaning that the friction factor from the SLA coupons decreases with

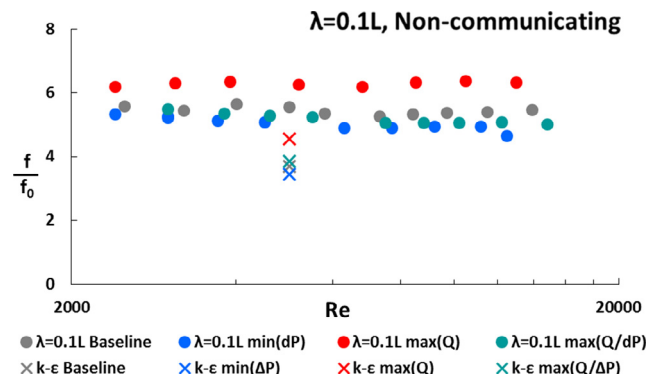


Fig. 10. Friction factor augmentation for the $\lambda = 0.1 L$ non-communicating (isolated) channel case. The smooth duct friction factor was calculated using the Colebrook formula [32].

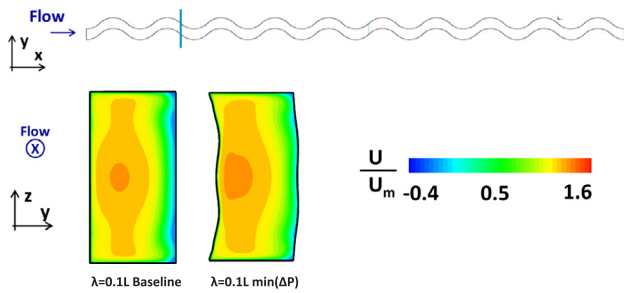


Fig. 11. 2D slices taken at 17.5% of the channel length of the $\lambda = 0.1$ L Baseline and min(ΔP) cases. Contours are colored with normalized axial velocity. Note that contours colored blue showcase flow moving in the negative x direction. (For interpretation of the references to colour in this figure legend, the reader is referred to the web version of this article.)

Reynolds number at the same rate as a perfectly smooth channel.

The magnitude of the experimental results differs from the numerical results by between 35 and 50%, which may be attributed to the inability of the flow solver to capture all secondary flows; the realizable $k-\epsilon$ turbulence model is known to fall short in capturing complex flows accurately [43].

However, the trends between experimental and numerical results were similar. For example, the channels optimized for a decrease in pressure loss showed a 5–9% decrease in friction factor augmentation experimentally. The numerical results predicted a 6% decrease in friction factor augmentation. In the simulation, the objective to minimize pressure loss was achieved by mitigating backflow in the channel, as mentioned in Section 5. Where the radius of curvature switched signs (shown in Fig. 1), the flow solver showed signs of backflow in the baseline case. Fig. 11 shows 2D slices at 20% of the channel length colored by normalized axial velocity. Two specific locations of backflow can be seen in the baseline contour, denoted by any dark blue color. In contrast, all fluid in the slice through the optimized channel is moving in the flow direction. These shape changes translated well to the experimental results, which indeed showed a decreased pressure loss relative to the baseline design.

The objective to maximize heat transfer also yielded similar friction factor augmentation trends in both experimental and numerical results. In the experimental results, the objective to maximize heat transfer showed a friction factor augmentation between 10 and 20% higher than the baseline; in the numerical results, the optimized channel showed a 25% increase in friction factor augmentation over the baseline.

As mentioned in Section 5, the intent of the shape optimization to increase the heat transfer revolved around creating stronger vortices in the channels [1]. Fig. 12 shows 2D slices taken from the numerical results at 55% of the channel length from the $\lambda = 0.1$ L baseline and

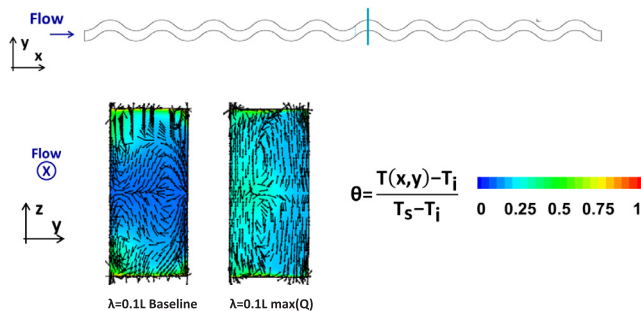


Fig. 12. 2D slices taken at 55% of the channel length of the $\lambda = 0.1$ L Baseline and max(Q) cases. Contours are colored with nondimensional temperature; secondary velocity vectors are overlaid. Note the direction of the secondary velocity vectors in the max(Q) case relative to the baseline case. (For interpretation of the references to colour in this figure legend, the reader is referred to the web version of this article.)

$\lambda = 0.1$ L max(Q) geometries. Note that slice locations Fig. 12 do not showcase any shape changes. All shape changes occurred in between the peaks and troughs of the wavy channels, where the radius of curvature switched signs, which strongly affected the flow structures in the peaks and troughs.

The contours in Fig. 12 are colored by non-dimensional temperature; secondary velocity vectors are included as well. The contour levels in the baseline case are noticeably darker (lower non-dimensional temperature) than in the case to maximize heat transfer. Additionally, the velocity vector directions differ significantly. Where heat transfer was to be maximized, velocity vectors pointed directly vertical, showing that fluid was forced toward the top and bottom endwalls to remove the heat. These vortical structures undoubtedly played a role in the friction factor increase over the baseline case, and their creation translated well to the experimental results.

The objective to maximize the ratio of heat transfer to pressure loss performed differently than predicted, in that the friction factor augmentation in the experimental results was lower than the baseline. The numerical simulation predicted a higher friction factor augmentation than the baseline. This discrepancy may be attributed to the flow solution's ill prediction of the vortex strength. In general, the shape changes for the objective to maximize the ratio of heat transfer to pressure loss were a compromise between those for the objective to maximize heat transfer and the objective to minimize pressure loss. In the experimental results, the strength of the vortices induced by the shape changes are hypothesized to have exerted a weaker effect on the friction factor than predicted; the shape changes that reduced backflow outweighed those that promoted stronger vortices.

Fig. 13 shows friction factor augmentation for both numerical and experimental results from the $\lambda = 0.4$ L configuration. Note that the abscissa is half that from Fig. 10; the friction factor augmentation in the longer wavelength was much less than for the shorter wavelength. Additionally, the difference in magnitude between the numerical and experimental results in Fig. 13 was significantly smaller than in Fig. 10. Given the longer distance the fluid traveled before reaching a sign change in the radius of curvature, the flow incurred fewer losses and was prone to fewer secondary flows. Characteristic Dean vortices form most fully in the peaks and troughs of the channels, fewer of which were present in the $\lambda = 0.4$ L case than in the $\lambda = 0.1$ L case. As such, the realizable $k-\epsilon$ model was able to capture the flow features more accurately than in the shorter wavelength.

The goals of the optimizer in the $\lambda = 0.4$ L case were structured around the secondary flows in the channels. Where pressure drop was to be minimized, the size of these vortices was diminished; where heat transfer was to be maximized, the size of these vortices was enhanced. Fig. 14 supports these claims. 2D slices are shown at the axial location specified in the figure, and show non-dimensional temperature contours with secondary velocity vectors overlaid. The fullest vortices are seen for the objective to maximize heat transfer, while the smallest are seen

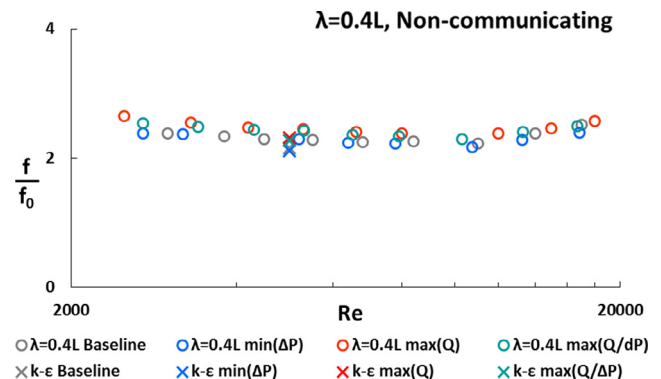


Fig. 13. Friction factor augmentation for the $\lambda = 0.4$ L non-communicating (isolated) channel case.

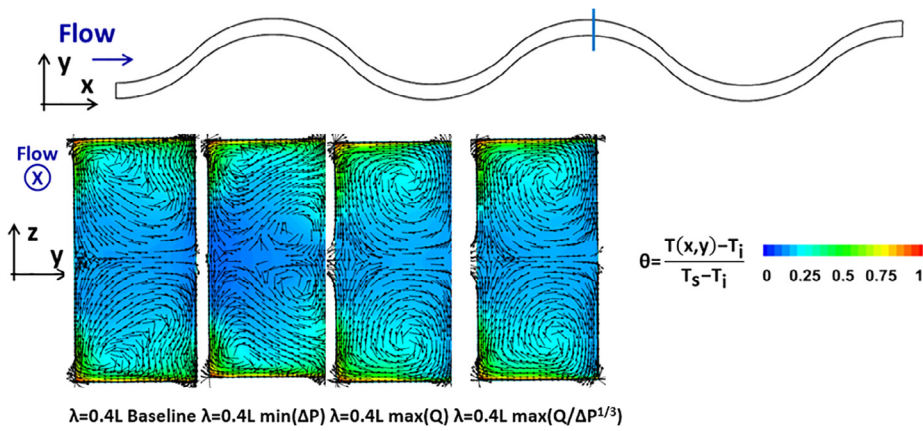


Fig. 14. 2D slices taken at 60% the channel length of the $\lambda = 0.4L$ design. The baseline and all three optimized cases are shown. Contours are colored with non-dimensional temperature; secondary velocity vectors are overlaid. (For interpretation of the references to colour in this figure legend, the reader is referred to the web version of this article.)

for the objective to minimize pressure loss. Given the longer flow development length, the amount of backflow in the $\lambda = 0.4L$ channels was negligible. Therefore, the predominant flow features to be targeted by the shape changes were the vortices. The non-dimensional temperature contour levels reflect the flowfield shown from the vectors. Stronger mixing, and therefore higher non-dimensional temperatures, were seen where the vortices are strongest.

The objective to maximize the ratio of heat transfer to pressure loss exhibited shape changes that closely mimicked those for the objective to maximize heat transfer. Fig. 14 shows very similar vortical structures in the objective to maximize the ratio of heat transfer to pressure loss as those seen in the objective to maximize heat transfer solely. The objective to maximize the ratio of heat transfer to pressure loss resulted in an increase in friction factor augmentation of 6% over the baseline, which matched the simulation results.

7.1.2. Communicating channels

Fig. 15 shows the friction factor augmentation for the communicating channels at the $\lambda = 0.1L$ wavelength. Much like in Fig. 10, the magnitude between the numerical and experimental results differed by 40–50%. However, the trends predicted by the simulations were again captured in the experimental results. The experimental results for the objective to maximize heat transfer showed a 4% increase in friction factor augmentation over the baseline, which was similar to the prediction of an increase by 5%. Additionally, the objective to minimize pressure loss yielded a friction factor 5% under the baseline, which again was markedly close to the simulation's result of a decrease by 4%.

The inclusion of the branches between wavy channels strongly influenced the formation of vortical structures in the primary channels. As such, the majority of shape changes in the communicating channels came in the vicinity of the branches. Fig. 16 shows 2D slices of all four $\lambda = 0.1L$ communicating channel cases at an axial distance of 65% the channel length. Unsurprisingly, the largest vortices are seen for the

objective to maximize heat transfer, as are the lowest non-dimensional temperatures. In looking at the objective to maximize the ratio of heat transfer to pressure loss, the vortices are present, but smaller in magnitude than those for the objective to maximize heat transfer only. By contrast, the secondary flows for the objective to minimize pressure loss are minimal. The shape changes generated by the optimizer can be hypothesized to have generated similar flow structures in SLA test coupons, given the similar trends seen in Fig. 15.

As was the case for the $\lambda = 0.4L$ non-communicating channels, the difference in friction factor augmentation between the numerical and experimental results for the $\lambda = 0.4L$ communicating channels was small. Fig. 17 shows the experimental and numerical friction factor augmentation results for the $\lambda = 0.4L$ communicating channels. Due to the branch pattern and the long wavelength of the primary channels, the number of branches in the test coupon was significantly smaller than in the $\lambda = 0.1L$ case (Fig. 2). Therefore, the increase in fluid mixing due to the branches, and thus an increase in the requirement for the realizable $k-\epsilon$ model to model stronger secondary flows, was nominal. The objective to minimize pressure loss was achieved in the experimental results, as was the objective to maximize heat transfer. The objective to maximize the ratio of heat transfer to pressure drop, however, deviated from the intended result. The strength of the vortices in the $\lambda = 0.4L$ communicating channels is hypothesized to be stronger than predicted, and thus yielded a higher friction factor augmentation than the baseline.

7.2. SLA test coupons vs. L-PBF coupons

As previously mentioned, the experimental results from the optimized L-PBF channels showed mixed success in terms of replicating the trends predicted by the simulation. The following discussion will delve into these discrepancies, and examine the influence of high surface roughness on the channels' performance by focusing on the $\lambda = 0.1L$ wavelength.

7.2.1. Non-communicating channels

Fig. 18 shows normalized friction factor from each of the optimized channels of the $\lambda = 0.1L$ non-communicating configuration. Experimental data from the L-PBF and SLA test coupons are included, as well as the results from the realizable $k-\epsilon$ simulation. Each data point is normalized by its respective baseline design.

The L-PBF test coupons failed at the objective to minimize pressure loss: the optimized channels showed a higher friction factor than the baseline design. The shape changes aimed to minimize the backflow in the channels, which did not work in the L-PBF channels. The high surface roughness on the internal channel walls negated any effect that the wall shape had on mitigating backflow; roughness features that protruded into the flow undoubtedly disturbed the flow, rendering the shape changes ineffective in reducing pressure loss. However, for

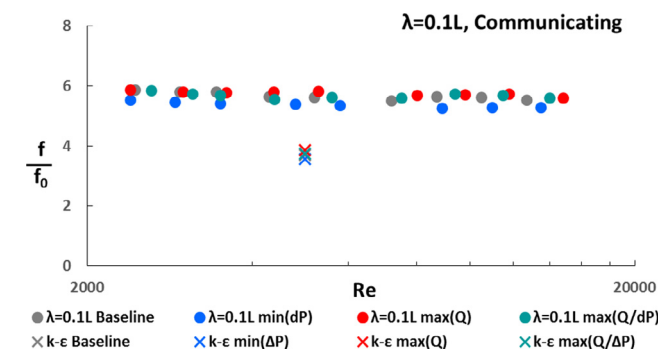


Fig. 15. Friction factor augmentation for the $\lambda = 0.1L$ communicating channel case.

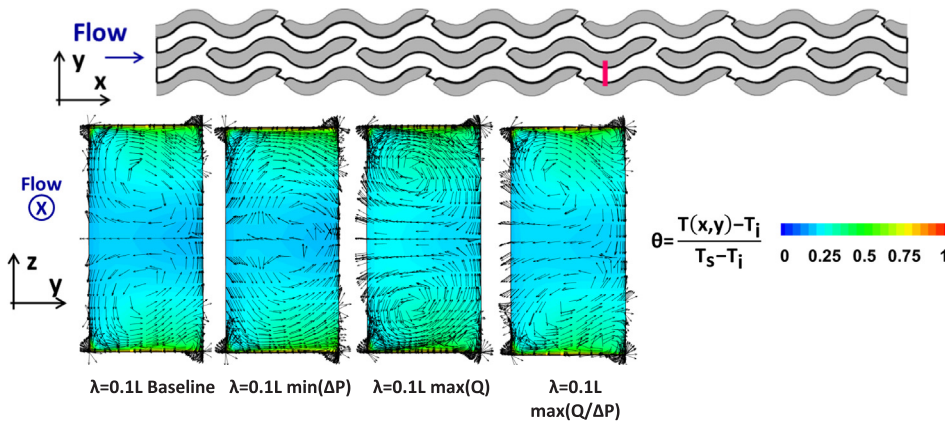


Fig. 16. 2D slices taken at 65% of the channel length of the $\lambda = 0.1 L$ communicating design. The baseline and all three optimized cases are shown. Contours are colored with non-dimensional temperature; secondary velocity vectors are overlaid. (For interpretation of the references to colour in this figure legend, the reader is referred to the web version of this article.)

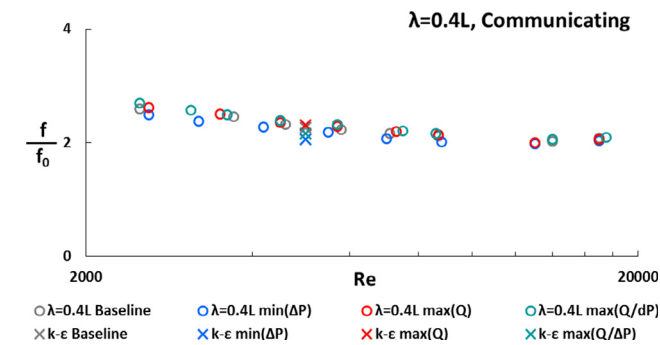


Fig. 17. Friction factor augmentation for the $\lambda = 0.4 L$ communicating channel case.

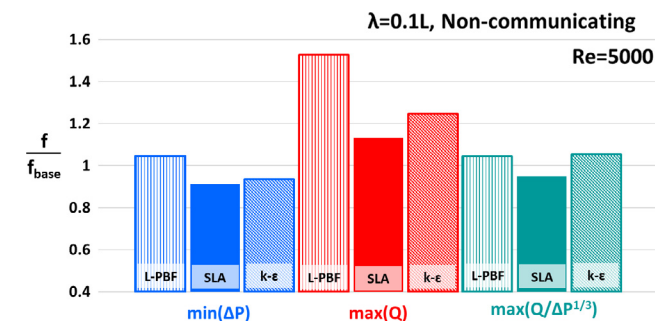


Fig. 18. Friction factor from the $\lambda = 0.1 L$ non-communicating L-PBF and SLA test coupons, as well as the realizable $k-\epsilon$ model, normalized by each configuration's respective baseline channel.

smooth-walled channels, the design intent was successfully achieved.

Where heat transfer was to be maximized, the optimized L-PBF microchannels showed a friction factor over 50% higher than the L-PBF baseline microchannels. The shape of the optimized channels was meant to encourage stronger vortex formation. Given the rough channel walls, this shape change in the L-PBF channels most likely augmented the design intent; the combination of larger-scale vortices, induced by the shape change, and smaller-scale vortices, induced by the roughness features, contributed to a friction factor well above the baseline.

The SLA coupon optimized for heat transfer, however, showed a lower normalized friction factor than the numerical model. This result supports the aforementioned claim that the flow solution most likely under predicted the strength of the vortices. The discrepancy between the realizable $k-\epsilon$ model and the SLA test coupon showcases just how much the roughness in the L-PBF microchannels amplified the design intent.

For the final objective to maximize the ratio of heat transfer to pressure loss, the L-PBF microchannel performance matched almost

exactly that of the numerical model; the performance of the SLA coupon, on the other hand, showed a lower normalized friction factor. An explanation for these results can take a similar form to that given for the results to maximize heat transfer: the numerical model under predicted the strength of the secondary flows in the channel. However, the surface roughness in the L-PBF channels enhanced vortex formation, which increased the friction factor. This design intent was, in fact, helped by the surface roughness because the goal to increase the fluid mixing was tempered by the goal to mitigate pressure loss. The optimized shape changes, in tandem with the surface roughness, led to the achievement of the design goal.

7.2.2. Communicating channels

The shape changes in the communicating channels were focused on the areas surrounding the branches, and as a result, generated different shape changes than in the non-communicating cases. As such, an analysis into the performance of the L-PBF communicating channels can lend further insight into the efficacy of the design tool.

Fig. 19 shows the friction factor from each of the optimized $\lambda = 0.1 L$ communicating channels, normalized by the baseline. As in Fig. 18, experimental results from the L-PBF and SLA test coupons are included, along with the results from the numerical simulation.

An unexpected result shown in Fig. 19 is that the L-PBF test coupon outperformed its numerical goal: the L-PBF coupon yielded a lower normalized friction factor than the realizable $k-\epsilon$ model predicted. In the optimized channels, the branch shapes were morphed such that they introduced flow into the neighboring branch at a shallow angle, thereby mitigating jet penetration. This shape change was much more transferable to the L-PBF manufacturing process than that to mitigate backflow, and proved much less sensitive to the addition of high surface roughness.

Additionally, the sharp exit of the branch in the initial design (seen in Fig. 2) did not build exactly as intended in the L-PBF test coupons

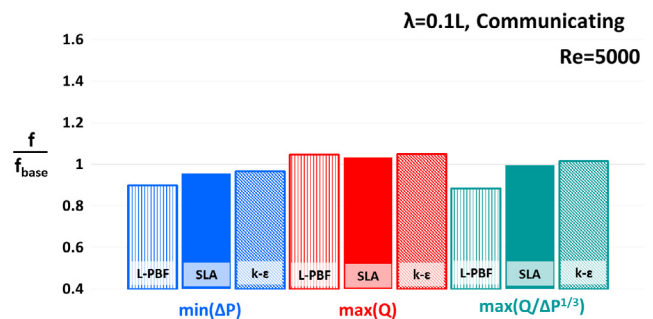


Fig. 19. Friction factor from the $\lambda = 0.1 L$ communicating L-PBF and SLA test coupons, as well as the realizable $k-\epsilon$ model, normalized by each configuration's respective baseline channel.

due to its small size, and to the build angle chosen [2]. Fig. 19 supports a hypothesis that the more easily-manufactured shape change, combined with the lack of intended jet penetration, led to a more successful representation of the optimized goal in the L-PBF channels. A similar hypothesis can be applied to the objective to maximize the ratio of heat transfer to pressure loss; the intended and unintended shape changes that mitigated jet penetration eclipsed those that sought to encourage fluid mixing.

The L-PBF microchannels optimized for heat transfer exhibited the same performance as intended. Again, most shape changes occurred near the branches, and served to intensify jet penetration. This shape change appeared to be less sensitive to the surface roughness than shape changes to promote stronger vortices. Due to the lack of sharp branch exit in the L-PBF coupons, the experimental results show that the surface roughness did not augment the intent to maximize heat transfer to the same magnitude as the non-communicating channels.

8. Conclusions

The genesis of the current study derived from a fundamental disconnect between numerical design tools and manufacturing processes. As additive manufacturing continues to generate excitement, the need for design tools that fully exploit its many capabilities will grow.

The current study used microchannel heat exchanger designs as the medium through which to investigate a simple, computationally-efficient optimization tool. The tool made of an adjoint-based sensitivity analysis, which informed shape change. Sensitivities of the design variables, which were comprised of every computational mesh node, were calculated using a steady flow solver, which was chosen to minimize the computational load. The optimization objectives were to (1) minimize the pressure loss between channel inlet and exit, (2) maximize the heat transfer on the top and bottom endwalls, and (3) maximize the ratio of heat transfer to pressure loss. Each objective was achieved numerically, and the resulting geometries were complex.

The four baseline and optimized wavy cooling channels were printed using a Stereolithography process that accurately replicated the designs. Two different wavelengths were studied; half of the test coupons contained channels that were isolated from one another, while the other contained communicating channels.

Experimental results showed that the design tool worked well. Despite the sensitivity analysis having been calculated from a steady flow solution, the chosen turbulence model captured enough flow features to generate a shape change that accomplished its goals experimentally. General weak points of the flow solver were found in its ability to capture the strengths of the vortices accurately.

This study also aimed to delve deeper into the results from previous studies in which the same optimized channels were manufactured using Laser Powder Bed Fusion. High surface roughness in these test coupons introduced flow features that were not taken into account in the simulation. Due to the surface roughness, shape changes that were particularly sensitive to surface roughness enhanced the friction factor well beyond its intended value. However, shape changes that were not as sensitive to roughness generated results that were comparable to the intent.

The fields of design and manufacturing are rapidly evolving. Tandem advances in both fields will lead to a closer link between an intended design and its manufactured part. Integrating the consequences of the additive process into design tools is an integral step in fully realizing the potential of the advanced manufacturing process. However, until such technology exists, an in-depth analysis of the current design tools can prove useful to those aiming for better, more efficient designs.

Acknowledgments

This work was financially supported by the National Science

Foundation Graduate Research Fellowship Program under Grant No. DGE1255832. The CT scans were performed by Jacob Snyder, from the Penn State Steady Thermal Aero Research Turbine Laboratory; the authors are incredibly grateful for his efforts.

References

- [1] K.L.K.L. Kirsch, K.A.K.A. Thole, Experimental investigation of numerically optimized wavy microchannels created through additive manufacturing, *J. Turbomach.* 140 (2) (2017) 21002.
- [2] K.L. Kirsch, K.A. Thole, Numerical Optimization, Characterization, and Experimental Investigation of Additively Manufactured Communicating Microchannels, ASME Paper No. GT2018-75429, 2018.
- [3] L. Martinelli, A. Jameson, Computational aerodynamics: solvers and shape optimization, *J. Heat Transfer* 135 (1) (2012) 11002.
- [4] E.M. Dede, S.N. Joshi, F. Zhou, Topology optimization, additive layer manufacturing, and experimental testing of an air-cooled heat sink, *J. Mech. Des.* 137 (11) (2015) 1–9.
- [5] S. Xu, D. Radford, M. Meyer, J.-D. Müller, CAD-Based Adjoint Shape Optimization of a One-Stage Turbine with Geometric Constraints, ASME Paper No. GT2015-42237, 2015.
- [6] K. Morimoto, Y. Suzuki, N. Kasagi, Optimal Shape Design of Compact Heat Exchangers Based on Adjoint Analysis of Momentum and Heat Transfer, *J. Therm. Sci. Technol.* 5 (1) (2010) 24–35.
- [7] Z. Lyu, J. Martins, RANS-Based Aerodynamic Shape Optimization of a Blended-Wing-Body Aircraft, in: Proc. 51st AIAA Aerosp., 2013, pp. 1–17.
- [8] J. Dirker, J.P. Meyer, Topology optimization for an internal heat-conduction cooling scheme in a square domain for high heat flux applications, *J. Heat Transfer* 135 (11) (2013) 111010.
- [9] M. Pietropaoli, R. Ahlfeld, F. Montomoli, A. Caini, M. D'Ercole, Design for Additive Manufacturing: Internal Channel Optimization, ASME Paper No. GT2016-57318, 2016.
- [10] S. Willeke, T. Verstraete, Adjoint Optimization of an Internal Cooling Channel U-Bend, ASME Paper No. GT2015-43423, ASME, 2015, pp. V05AT11A029 (13 pages).
- [11] T. Verstraete, S. Amaral, R. Van den Braembussche, T. Arts, Design and optimization of the internal cooling channels of a high pressure turbine blade—Part II: optimization, *J. Turbomach.* 132 (2) (2010) 21013.
- [12] J.C. Snyder, C.K. Stimpson, K.A. Thole, D. Mongillo, Build direction effects on additively manufactured channels, *J. Turbomach* 138 (5) (2016) 051006 (10 pages).
- [13] C.K. Stimpson, J.C. Snyder, K.A. Thole, D. Mongillo, Roughness effects on flow and heat transfer for additively manufactured channels, *J. Turbomach.* 138 (5) (2016) 051008 (13 pages).
- [14] R.J. Norris, Some Simple Approximate Heat Transfer Correlations for Turbulent Flow in Ducts with Surface Roughness, American Society of Mechanical Engineers M4 - Citavi, New York, 1971.
- [15] I. Yadroitsev, I. Smurov, Surface morphology in selective laser melting of metal powders, *Phys. Proc.* 12 (1) (2011) 264–270.
- [16] P.B. Bacchewar, S.K. Singhal, P.M. Pandey, Statistical modelling and optimization of surface roughness in the selective laser sintering process, *Proc. Inst. Mech. Eng. Part B-J. Eng. Manuf.* 221 (1) (2007) 35–52.
- [17] J. Pakkanen, F. Calignano, F. Trevisan, M. Lorusso, E.P. Ambrosio, D. Manfredi, P. Fino, Study of internal channel surface roughnesses manufactured by selective laser melting in aluminum and titanium alloys, *Metall. Mater. Trans. A* 47 (3837) (2016).
- [18] J. Delgado, J. Giurana, C.A. Rodríguez, Influence of process parameters on part quality and mechanical properties for DMLS and SLM with iron-based materials, *Int. J. Adv. Manuf. Technol.* 60 (5–8) (2012) 601–610.
- [19] B. Dai, M. Li, Y. Ma, Effect of surface roughness on liquid friction and transition characteristics in micro- and mini-channels, *Appl. Therm. Eng.* 67 (1) (2014) 283–293.
- [20] K. Huang, J.W. Wan, C.X. Chen, Y.Q. Li, D.F. Mao, M.Y. Zhang, Experimental investigation on friction factor in pipes with large roughness, *Exp. Therm. Fluid Sci.* 50 (2013) 147–153.
- [21] S.G. Kandlikar, D. Schmitt, A.L. Carrano, J.B. Taylor, Characterization of surface roughness effects on pressure drop in single-phase flow in minichannels, *Phys. Fluids* 17 (2005) (2005) 100606.
- [22] C.K. Stimpson, J.C. Snyder, K.A. Thole, Scaling roughness effects on pressure loss and heat transfer of additively manufactured channels, *J. Turbomach.* 139 (2) (2016) 021003 (10 pages).
- [23] P.K. Singh, S.H.F. Tan, C.J. Teo, P.S. Lee, Flow and Heat Transfer in Branched Wavy Microchannels, ASME Paper No. MNHMT2013-22058, 2013.
- [24] S.W. Chang, A.W. Lees, T.C. Chou, Heat transfer and pressure drop in furrowed channels with transverse and skewed sinusoidal wavy walls, *Int. J. Heat Mass Transf.* 52 (19–20) (2009) 4592–4603.
- [25] M.V. Pham, F. Plourde, S.K. Doan, Turbulent heat and mass transfer in sinusoidal wavy channels, *Int. J. Heat Fluid Flow* 29 (5) (2008) 1240–1257.
- [26] Y. Sui, C.J. Teo, P.S. Lee, Y.T. Chew, C. Shu, Fluid flow and heat transfer in wavy microchannels, *Int. J. Heat Mass Transf.* 53 (13–14) (2010) 2760–2772.
- [27] A.M. Guzmán, M.J. Cárdenas, F.A. Urzúa, P.E. Araya, Heat transfer enhancement by flow bifurcations in asymmetric wavy wall channels, *Int. J. Heat Mass Transf.* 52 (15–16) (2009) 3778–3789.
- [28] K.L. Kirsch, K.A. Thole, Heat transfer and pressure loss measurements in additively manufactured wavy microchannels, *J. Turbomach.* 139 (1) (2017) 11007.
- [29] A.M. Weaver, J. Liu, T.I. Shih, A Weave Design for Trailing-Edge Cooling, AIAA-

- 2015-1446, 2015.
- [30] Pointwise, Pointwise, 2015.
- [31] ANSYS, ANSYS FLUENT, 2015.
- [32] C.F. Colebrook, C.M. White, Experiments with fluid friction in roughened pipes, *Proc. Roy. Soc. Lond. A. Math. Phys. Sci.* 161 (906) (1937) 367–381.
- [33] V. Gnielinski, New equations for heat and mass transfer in turbulent pipe and channel flow, *Int. Chem. Eng.* 16 (2) (1975) 359–368.
- [34] D.L. Gee, R.L. Webb, Forced convection heat transfer in helically rib-roughened tubes, *Int J Heat Mass Transf.* 23 (1980) 1127–1136.
- [35] Formlabs, FormLabs 2, 2016.
- [36] EOS GmbH, EOS NickelAlloy IN718 for EOSINT M 270 Systems, 2014, p. 6 T4-Material data sheet M4.
- [37] M.W. Khaing, J.Y.H. Fuh, L. Lu, Direct metal laser sintering for rapid tooling: processing and characterisation of EOS parts, *J. Mater. Process. Technol.* 113 (1–3) (2001) 269–272.
- [38] EOS GmbH, EOSINT M 280 System Data Sheet.
- [39] Volume Graphics MAX, 2014.
- [40] AliCat, Mass Flow Controller - Operating Manual, 2014.
- [41] H.L. Langhaar, Steady flow in the transition length of a straight tube, *J. Appl. Mech.* 9 (1942) A55–A58.
- [42] S.J. Kline, F.A. McClintock, Describing the uncertainties in single sample experiments, *Mech. Eng.* 75 (1953) (1953) 3–8.
- [43] S.B. Pope, *Turbulent Flows*, Cambridge University Press, 2000.